Cell Reports
Physical Science

Article

Finding lanthanide magnetic anisotropy axes in 3d-4f butterfly single-molecule magnets using inelastic neutron scattering

Graphical abstract

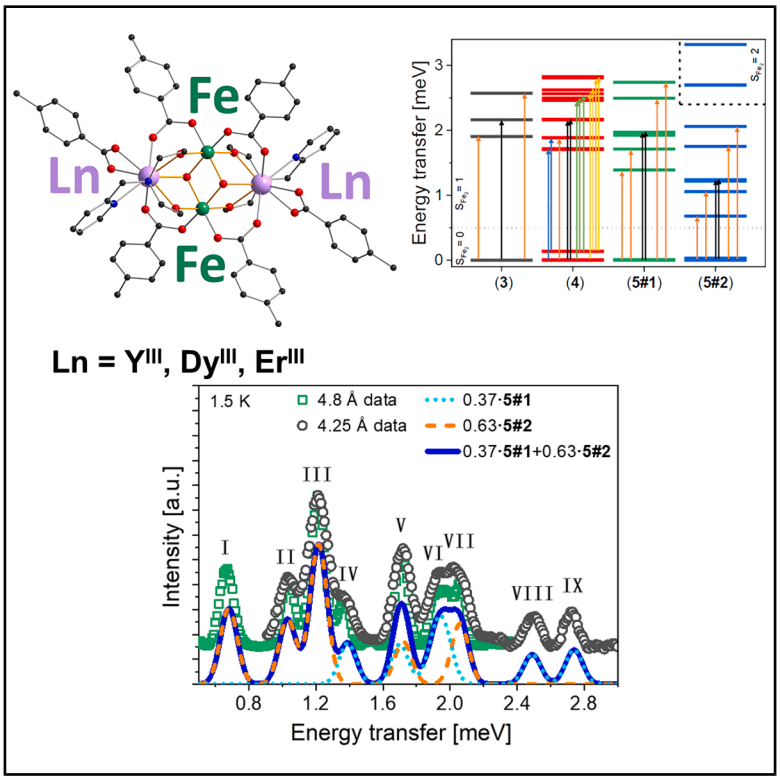

Authors

Julius Mutschler, Thomas Ruppert, Yan Peng, ..., Mario Ruben, Annie K. Powell, Oliver Waldmann

Correspondence

oliver.waldmann@physik.uni-freiburg.de (O.W.), annie.powell@kit.edu (A.K.P.)

In brief

Mutschler et al. report an in-depth study on Fe_2Ln_2 butterfly coordination clusters in which they used inelastic neutron scattering to determine the magnetic anisotropy axes. Models for the description are developed, reproduce the experimental data excellently, and thus provide benchmarks to test *ab initio* calculations.

Highlights

- 3d-4f clusters combine the advantages of both types of metal ions
- Magnetic anisotropy is key for single-molecule magnets
- Inelastic neutron scattering on powder can provide information on anisotropy directions
- No deuteration was necessary as a result of the strong magnetic transitions of the 3d ions

Mutschler et al., 2025, Cell Reports Physical Science 6, 102848
October 15, 2025
https://doi.org/10.1016/j.xcrp.2025.102848

CellPress

Cell Reports
Physical Science

CellPress
OPEN ACCESS

Article

Finding lanthanide magnetic anisotropy axes in 3d-4f butterfly single-molecule magnets using inelastic neutron scattering

Julius Mutschler,[1] Thomas Ruppert,[2] Yan Peng,[2,3] Sören Schlittenhardt,[4] Yannik F. Schneider,[2,4] Jonas Braun,[2,4,5] Christopher E. Anson,[2] Jacques Ollivier,[6] Quentin Berrod,[7] Jean-Marc Zanotti,[8] Mario Ruben,[4,5,9] Annie K. Powell,[2,4,5,*] and Oliver Waldmann[1,10,*]

[1]Physikalisches Institut, Universität Freiburg, Hermann-Herder-Strasse 3, 79104 Freiburg, Germany
[2]Institute of Inorganic Chemistry, Karlsruhe Institute of Technology, Kaiserstrasse 12, 76131 Karlsruhe, Germany
[3]School of Chemistry and Chemical Engineering, Jiangxi Provincial Key Laboratory of Functional Crystalline Materials Chemistry, Jiangxi University of Science and Technology, Ganzhou, Jiangxi 341000, P.R. China
[4]Institute of Nanotechnology, Karlsruhe Institute of Technology, Kaiserstrasse 12, 76131 Karlsruhe, Germany
[5]Institute of Quantum Materials and Technologies, Karlsruhe Institute of Technology, Kaiserstrasse 12, 76131 Karlsruhe, Germany
[6]Institut Laue-Langevin, 38042 Grenoble Cedex 9, France
[7]Univ. Grenoble Alpes, CNRS, CEA, Grenoble INP, IRIG, SyMMES, Grenoble, France
[8]Université Paris-Saclay, CEA, CNRS, Laboratoire Léon Brillouin, CEA Saclay, Gif-sur-Yvette, France
[9]Centre Européen de Sciences Quantiques (CESQ), Institut de Science et d'Ingénierie Supramoléculaires (ISIS), 8 Allée Gaspard Monge, BP 70028, 67083 Strasbourg Cedex, France
[10]Lead contact
*Correspondence: oliver.waldmann@physik.uni-freiburg.de (O.W.), annie.powell@kit.edu (A.K.P.)
https://doi.org/10.1016/j.xcrp.2025.102848

SUMMARY

A fundamental aspect of lanthanide-containing single-molecule magnets (SMMs) is determining the orientation of the magnetic anisotropy axes. However, the experimental determination is challenging. Here, we present an inelastic neutron scattering (INS) study on a family of 3d-4f $M^{III}_2Ln^{III}_2$ butterfly compounds, with M = Al^{III} or Fe^{III} and Ln^{III} = Y^{III}, Er^{III}, or Dy^{III}. The rich INS spectra presented here provide significantly more experimental information in comparison to those of pure 4f clusters. As a main result, for Fe_2Er_2 and Fe_2Dy_2, the relative angle between the Ln^{III} and the Fe^{III} main anisotropy axes is determined. Models for the description of the magnetic properties are developed and found to reproduce the INS data, as well as the magnetic susceptibility and magnetization curves, with good accuracy. The results provide benchmarks for testing high-level *ab initio* theoretical approaches.

INTRODUCTION

The discovery of slow magnetic relaxation and quantum tunneling of magnetization in single-molecule magnets (SMMs) three decades ago triggered intense research into their magnetic properties.[1–3] For practical applications of SMMs, such as in quantum information technologies or data storage,[4–12] the blocking temperature T_B, below which SMM behavior is observed, has to be somehow increased. It was shown that the total spin S of the cluster is not the most important parameter for achieving a high T_B, but the single-ion anisotropies of the incorporated paramagnetic centers are.[13,14] Accordingly, focus has shifted toward synthesizing and studying molecular clusters containing strongly anisotropic metal ions, such as lanthanides, and remarkable progress has been made.[15–20] For instance, a T_B exceeding liquid nitrogen temperature was observed in a mononuclear dysprosium metallocene SMM.[21–24] The blocking temperature is, along with other factors such as molecular vibrations or spin-phonon coupling strengths,[25,26] related to the details of the magnetic energy spectrum as well as wave functions generated by the single-ion anisotropies and possible exchange interactions between the paramagnetic centers.[27–30] In addition to the SMMs, the class of magnetic molecules exhibiting toroidal magnetic moments has recently attracted much interest, since systems with exotic quantum states carrying toroidal moments could lead to novel applications.[31–38] Understanding the interplay between single-ion anisotropies and exchange interactions, including the orientations of single-ion magnetic anisotropy axes, is thus of paramount relevance for furthering the field.

Inelastic neutron scattering (INS) has been demonstrated to be an excellent experimental tool for studying both magnetic exchange interactions and single-ion magnetic anisotropies in molecular clusters containing 3d metal ions.[39–41] Recently, a few 4f-based single-ion magnets (SIMs) and polynuclear 4f SMMs have also been successfully studied by INS.[42–48] However, INS experiments on polynuclear pure 4f SMMs are challenging because of weak magnetic scattering intensities in comparison to the intensity of non-magnetic scattering mechanisms, such as spin-incoherent scattering or phonon scattering, or huge neutron absorption, especially in case of Dy.[48,49] Accordingly,

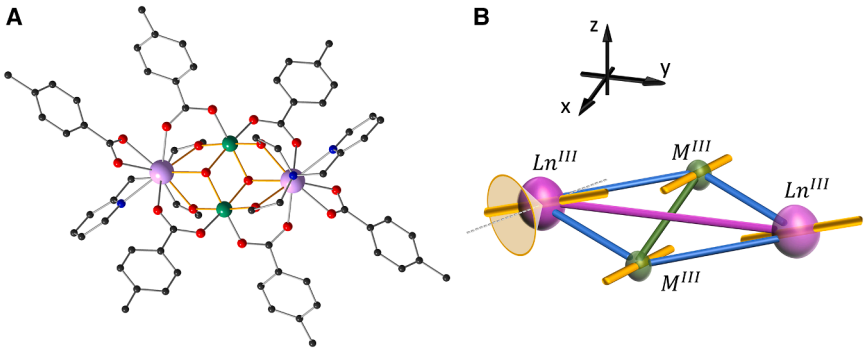

Figure 1. Molecular structure and scheme illustrating the magnetic model

(A) Ball-and-stick representation of the structure of the M_2Ln_2 butterflies. Green, M^{III} ions; pink, Ln^{III} ions; blue, nitrogen; red, oxygen; black, carbon. Hydrogen atoms are omitted for clarity.

(B) Sketch of the magnetic model. Magnetic ions are plotted in the same color as in (A). Blue lines, J_{3d-4f}; green line, J_{3d-3d}; pink line, J_{4f-4f}; yellow sticks, directions of the main anisotropy axes, with directions consistent with experiment (for details see text). The cone reflects the orientations of the Ln^{III} anisotropy axes, which are consistent with the relative angle $\tilde{\theta}$ in reference to the Fe^{III} anisotropy axes. The black arrows indicate the *x*, *y*, and *z* coordinate frame. It was chosen such that the M^{III} and Ln^{III} ions span the *xy* plane.

the experiments frequently require deuterated samples in order to suppress the large spin-incoherent scattering of hydrogen[50] and obtain sufficiently clear magnetic INS signals. Furthermore, it is often the case that only relatively few magnetic peaks can be observed. This poses a challenge in terms of the amount of information that can be deduced from the experiment.

Studying 3d-4f heterometallic molecules[29,49,51–55] can offer several advantages in this context. As will be demonstrated in this work, the magnetic scattering intensity in the energy range of up to a few meV can be dominated by the scattering from the 3d metal ions, and comparatively strong INS signals be observed even from non-deuterated samples. Furthermore, the magnetic interactions between the 3d and the 4f ions often lead to richer INS spectra yielding more information. In addition, information on the single-ion anisotropy axes can be obtained from the data, even when recorded on powder samples. In order to increase the amount of experimental information, it is beneficial to study series of isostructural molecules, where the 4f and/or 3d ions are substituted with various members of the periodic table, including diamagnetic ions.

This work reports an extensive INS study on five members of the family of molecules $[M^{III}_2Ln^{III}_2(\mu_3\text{-OH})_2(pmide)_2(p\text{-Me-PhCO}_2)_6]\cdot 2MeCN$ ($pmideH_2$ = N-(2-pyridylmethyl)-iminodiethanol), or M_2Ln_2 in short. Here, M can be Fe or Al, and Ln can be Er, Dy, or Y.[56,57] The molecular structure, shown in Figure 1A, is a typical butterfly structure, where the 3d metal ions form the body and the 4f ions the wings of the butterfly. Some of us have previously reported on these and other closely related butterfly cluster molecules. Although they are not themselves what would be regarded as "high-performance" SMMs,[58] the relative simplicity of the structural motif and the wide range of possibilities to modify it has made such clusters an ideal test-bed system for fundamental studies on the magnetic behavior of 3d-4f SMMs. For example, the studies have shown the sensitivity of the ligand field around Dy^{III} centers to remote changes in ligand substituents,[59] the interplay between the various magnetic couplings within the butterflies and their SMM properties,[60,61] and the different timescales of the various relaxation processes involved.[56] The results of such studies provide a theoretical background,[54] which could then be applied to high-performance 3d-4f SMMs, which would, by reason of their more complicated structures, not be amenable to such fundamental studies.

The INS spectra were recorded on non-deuterated powder samples of Al_2Er_2 (**1**), Al_2Dy_2 (**2**), Fe_2Y_2 (**3**), Fe_2Er_2 (**4**), and Fe_2Dy_2 (**5**). Al^{III} and Y^{III} are diamagnetic, and the first three compounds thus serve as model systems for the main subjects of the study, which are Fe_2Dy_2 and Fe_2Er_2. The compounds Al_2Er_2 and Al_2Dy_2 provide insight into the 4f single-ion magnetic spectrum in the experimental window and also the non-magnetic scattering contribution. The compound Fe_2Y_2 essentially represents a 3d dimer and permits an independent assessment of the Fe^{III}-Fe^{III} exchange interaction and the Fe^{III} single-ion anisotropy. The INS studies are complemented by temperature-dependent magnetic susceptibility and field-dependent magnetization curves.

It is shown that the INS measurements permit us to determine the main magnetic anisotropy directions of the Fe^{III} and Ln^{III} ions relative to each other in the compounds Fe_2Er_2 (**4**) and Fe_2Dy_2 (**5**), whereas for Fe_2Y_2 (**3**), the orientation of the Fe^{III} main anisotropy axis in relation to the molecular structure could be deduced. Recently, information on the local anisotropy axes in SMMs was obtained through the measurement of the local susceptibility tensor using polarized neutron diffraction (PND)[62–65] or high-resolution X-ray diffraction with a multipole model.[66] INS complements these techniques by providing experimental benchmarks for high-level theoretical methods that can yield directions of the main anisotropy axes, such as various *ab initio* approaches.[29,31,67–69]

RESULTS

Crystal structures

The samples of compounds **1–5** used for the INS measurements were examined by powder X-ray diffraction (PXRD) to determine the polymorphic phase(s) present, since the INS data are sensitive to the nature of the different polymorphic structures (see detailed discussion of the different polymorphs of the crystal structures of **1–5** in the supplemental information). To summarize, for both Fe_2Y_2 (**3**) and Fe_2Er_2 (**4**), the PXRD patterns showed that these two compounds were exclusively present as polymorph B (Figure S3). However, the INS sample of Fe_2Dy_2 (**5**) was found to be a mixture of polymorphs A (**5-A**) and B (**5-B**) in comparable amounts (Figure S4), where, e.g., **5-A** denotes compound **5** crystallizing in polymorph A. The INS sample of Al_2Er_2 (**1**) was prepared in several batches. Most of these were shown by PXRD to be a consistent mixture of polymorphs B and E

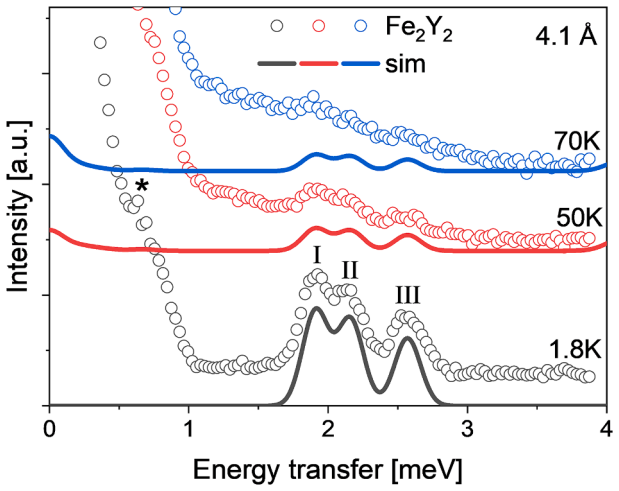

Figure 2. Neutron energy loss INS spectra for Fe_2Y_2 (3)

Data recorded with λ = 4.1 Å at T = 1.8 K (black dots), 50 K (red dots), and 70 K (blue dots) and simulated curves. Datasets were shifted for clarity. The asterisk marks an instrumental spurion. Three cold transitions, I, II, and III, are detected. The simulated curves, shown as solid lines with colors matching those of the associated experimental data, were calculated using Equation 2 with the parameters given in the main text.

(Figure S5) and were combined. Al_2Dy_2 (**2**) gave similar results. No traces of the polymorphs C and D could be detected in any of the samples.

Fe_2Y_2

Figure 2 shows experimental INS spectra for compound Fe_2Y_2 (**3**), recorded on the spectrometer IN6-SHARP with incident neutron wavelength λ = 4.1 Å, at temperatures T = 1.8, 50, and 70 K. At the lowest temperature, three peaks are clearly observed at energies of 1.90(5) meV (peak I), 2.15(5) meV (peak II), and 2.56(5) meV (peak III). A further weak feature is observed at 0.6(1) meV (marked by an asterisk), which will be identified as a spurion below. The intensities of the three peaks decrease with increasing temperature, which identifies them as cold magnetic transitions (transitions from the ground state to higher-lying states). Hot magnetic transitions are not observed (transitions from higher-lying states to higher- or lower-lying states). In the neutron energy gain spectra, the expected anti-Stokes transitions are observed, with further transitions in the range of −4 to −5 meV (Figure S6A). The $S(Q,\omega)$ plot, shown in Figure S6B, confirms the assignment of peaks I to III: the Q dependence of their scattering intensities unambiguously identifies them as of magnetic origin. The feature at 0.6 meV is unambiguously identified as spurious. The observed peaks I to III are characteristic of singlet S = 0 to triplet S = 1 transitions, with the triplet exhibiting zero-field splitting.[40] The transitions observed in the neutron energy gain range of 4–5 meV correspond to triplet S = 1 to quintet S = 2 transitions.[40]

The magnetic susceptibility data (Figure S7) exhibit the behavior characteristic of a dimer of high-spin Fe^{III} ions (S = 5/2, g = 2) with antiferromagnetic Heisenberg exchange coupling.[27] χT continuously decreases from a room temperature value of 6.5 emu K mol^{-1} to become essentially zero at the lowest temperature of T = 2 K, indicative of a total spin singlet S = 0 ground state. The magnetization curves (not shown) at low temperatures are very small, much smaller than the saturation magnetization of 10 μ_B expected for two uncoupled Fe^{III} ions, as expected for a non-magnetic, singlet ground state.

Both the INS and the magnetic data consistently point to an antiferromagnetically coupled spin-5/2 dimer with magnetic anisotropy, as expected from the molecular structure and consistent with previous magnetic analyses.[56,57] The energy scheme inferred from the observed INS transitions is presented in Figure 6.

Fe_2Er_2 and Al_2Er_2

Figure 3A presents experimental INS spectra for the Er-containing compounds Al_2Er_2 (**1**) and Fe_2Er_2 (**4**), recorded on the spectrometer IN6-SHARP with incident neutron wavelength λ = 5.1 Å, at temperatures T = 1.5 and 30 K. For both compounds, a weak feature at ∼0.8 meV (marked by an asterisk) is observed, which can be associated with a spurion. For compound Al_2Er_2 (**1**), magnetic scattering intensity was not observed in the experimental window of transfer energies of up to 10 meV. This implies that the ligand-field transitions expected for Er^{III} ions are either higher in energy than ∼10 meV or buried by non-magnetic scattering. These spectra thus reflect the scattering intensity from the non-magnetic contributions such as spin-incoherent or phononic scattering, and the data can be conveniently used to estimate the non-magnetic INS background in the measurements on compound Fe_2Er_2 (**4**).

For compound Fe_2Er_2 (**4**), five clear peaks are observed at 1.61 (1) meV (peak I), 1.88(1) meV (peak II), 2.17(1) meV (peak III), 2.39 (3) meV (peak IV), and 2.61(1) meV (peak V). A further very weak feature is observed at ∼1.4 meV (labeled P1). The temperature dependence of the scattering intensities of the five peaks are shown in detail in Figure S8A. The intensities of peaks I, II, III, and V decrease with increasing temperature, which identifies them as cold transitions of magnetic origin. The $S(Q,\omega)$ plot, shown for compound Fe_2Er_2 (**4**) in Figure 3B, confirms this assignment. The Q dependence of the scattering intensities unambiguously evidences their magnetic origin. The weak feature at ∼0.8 meV can clearly be identified as spurious. The assignments of peak IV and feature P1 are less clear. The temperature dependencies of their intensities are consistent with a magnetic origin, but the scattering intensity is very small, and the Q dependencies, while not well borne out, could be consistent with a phononic origin. Peak IV is significantly stronger than P1 and also clearly observed at 30 K, which could suggest a magnetic origin, while P1 appears to be most likely of extrinsic nature.

The neutron energy gain spectra are shown in Figure S9A. In the data of compound Fe_2Er_2 (**4**), two marked hot features in the ranges of −1.5 to −3 and −3.8 to −5 meV are observed. The feature at lower transfer energy can clearly be associated with the anti-Stokes transitions corresponding to the above-mentioned magnetic peaks. The other feature at more negative transfer energy stems from hot magnetic transitions, which were not observed in the neutron energy gain spectra due to high transfer energies. The magnetic origin of both features will be confirmed by simulations (*vide infra*).

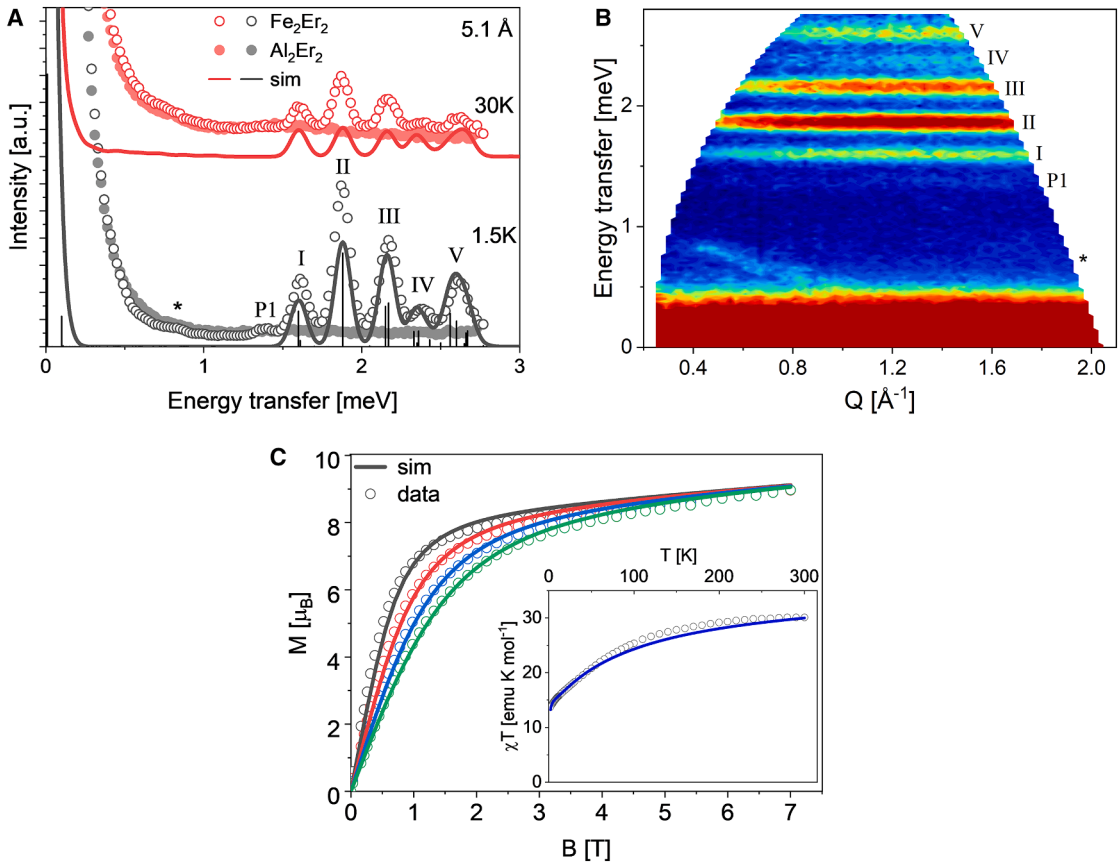

Figure 3. Experimental data for Fe_2Er_2 (4) and Al_2Er_2 (1) and simulations

(A) Neutron energy loss INS spectra recorded with λ = 5.1 Å at T = 1.5 K (black) and 30 K (red). The data for Al_2Er_2 (**1**) and Fe_2Er_2 (**4**) are represented by solid and open circles, respectively. Datasets were shifted for clarity. The asterisk marks a spurious feature. Five cold magnetic peaks, I, II, III, IV, and V, and a feature, P1, are observed in the Fe_2Er_2 (**4**) data. The Al_2Er_2 (**1**) data show no magnetic features. The results of simulations are shown as solid lines with colors matching those of the associated experimental data. For T = 1.5 K, the simulated spectrum with assumed zero line width is also shown as bars.

(B) $S(Q,\omega)$ plot for Fe_2Er_2 (**4**) recorded at T = 1.5 K with λ = 5.1 Å.

(C) Magnetization vs. applied field at T = 2 K (black), 3 K (red), 4 K (blue), and 5 K (green). The inset shows the susceptibility plotted as χT vs. temperature. Experimental data are represented by open circles. The simulated curves are shown as solid lines with colors matching those of the associated experimental data.

In all plots, the simulated curves were calculated using Equation 3 with the parameters given in the main text.

Figure 3C presents the magnetization curves for compound Fe_2Er_2 (**4**), and the inset shows the magnetic susceptibility data as a χT product. At T = 300 K, the χT value is 26.9 emu K mol^{-1}, which is lower than the value of 31.7 emu K mol^{-1} as calculated from the Curie constants C = 4.38 emu K mol^{-1} and C = 11.48 emu K mol^{-1} for free Fe^{III} and Er^{III} (J = 15/2, g_J = 1.2) ions, respectively. With decreasing temperature χT decreases, with a steeper decrease at temperatures below T ~8 K, and reaches a value of 11.8 emu K mol^{-1} at the lowest temperature of T = 2 K. This behavior is indicative of a thermal depopulation of the ligand-field states of the lanthanide ions and the possible presence of antiferromagnetic interactions. The magnetization curves initially increase linearly with magnetic field but approach saturation for the measured temperatures at the highest field, with a maximum value of 7.85(3) μ_B at B = 7 T. This clearly suggests a magnetic ground state of the cluster. The maximal magnetization is, however, significantly smaller than the theoretical value of 28 μ_B expected for free Fe^{III} and Er^{III} ions, indicating the presence of substantial magnetic anisotropy in the ground state and the potential effect of antiferromagnetic interactions. Given that for Al_2Er_2 (**1**) magnetic features were not observed in the INS spectra, the magnetic data of this compound were found to be of little relevance for this study and are thus not further discussed.

Fe_2Dy_2 and Al_2Dy_2

In Figure 4, the magnetic data recorded on compound Fe_2Dy_2 (**5**) are shown in detail. Figure 4A presents the magnetic susceptibility as the χT product in the full measurement range; the inset provides a zoom into the low temperature range. The χT value at T = 300 K is 37.6 emu K mol^{-1}, which is close to the value 37.1 emu K mol^{-1} as calculated from the Curie constants C = 4.38 emu K mol^{-1} and C = 14.17 emu K mol^{-1} for free Fe^{III} and Dy^{III} (J = 15/2, g_J = 4/3) ions, respectively. With decreasing temperatures, χT first decreases slowly, to pass a "kink" at T ~7 K, below which χT decreases significantly faster, reaching a value

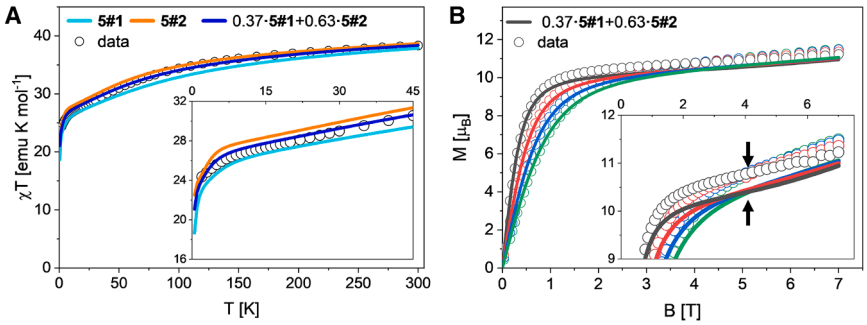

Figure 4. Experimental magnetic data for Fe_2Dy_2 (5) and simulated curves

(A) Susceptibility plotted as χT vs. temperature (open circles). The solid lines show the simulated susceptibility curves for species **5#1** (orange), species **5#2** (cyan), and the combined sample Fe_2Dy_2 (**5**) (blue), with composition as given in the main text.

(B) Magnetization vs. applied magnetic field at $T = 2$ K (black), 3 K (red), 4 K (blue), and 5 K (green). Experimental data are represented by open circles. The solid lines show the simulated susceptibility curves for the combined sample Fe_2Dy_2 (**5**), with composition as given in the main text and colors matching those of the associated experimental data. The inset shows the high field range in detail. The black arrows indicate a crossing point at $B \sim 4.1$ T. In all plots, the simulated curves were calculated using Equation 3 with the parameters given in the main text.

of 24.3 emu K mol^{-1} at T = 2 K. The behavior resembles that observed for compound Fe_2Er_2 (**4**), with similar conclusions concerning thermal depopulation of lanthanide ligand-field states and antiferromagnetic interactions in the system.

In Figure 4B the magnetization curves are shown in the full measurement range; the inset provides a zoom into the magnetization at higher fields. Similar to compound Fe_2Er_2 (**4**), the magnetization curves initially increase linearly with magnetic field and approach saturation at the highest field, clearly suggesting a magnetic ground state in Fe_2Dy_2 (**5**). The maximum value at T = 2 K and B = 7 T is 11.2 μ_B, which is substantially smaller than the theoretical value of 30 μ_B for free Fe^{III} and Dy^{III} ions and indicates substantial magnetic anisotropy in the ground state and the potential effects of antiferromagnetic interactions. In contrast to compound Fe_2Er_2 (**4**), however, a crossing of the magnetization curves at $B \sim 4.1$ T is observed, as detailed in the inset in Figure 4B. This suggest the presence of a relatively low-lying level in Fe_2Dy_2 (**5**) giving rise to a field-induced level crossing.

Figure 5 presents in detail experimental INS data for the Dy-containing compounds Al_2Dy_2 (**2**) and Fe_2Dy_2 (**5**), recorded on the spectrometer IN5 with incident neutron wavelengths λ = 4.25 and 4.8 Å, at temperatures of T = 1.5, 5, and 15 K. For compound Al_2Dy_2 (**2**), the spectra exhibit features, especially in the λ = 4.25 Å spectra, but all scattering intensity can be assigned to non-magnetic scattering based on the temperature and Q dependence of the intensities and the overall weak intensity. The features observed in the λ = 4.25 Å spectra at ~1.5 meV (labeled P2), ~2.0 meV (labeled P3), ~2.3 meV (labeled P4), and ~3.0 meV (labeled P5) can be assigned to spurious or non-magnetic origin: P2 is weakly temperature dependent and consistent with the Bose temperature dependence of phonons. P4 is clearly a spurion from the Q dependence. P3 and P5 are not temperature dependent and present in all spectra at this neutron wavelength, identifying them as spurious, too. The spectrum recorded for λ = 4.8 Å at T = 1.5 K is much cleaner, with only very minor features and the spurious feature P4. Thus, for compound Al_2Dy_2 (**2**), conclusions similar to those for compound Al_2Er_2 (**1**) can be drawn concerning the ligand-field transitions and that these spectra can be conveniently used to estimate the non-magnetic scattering contribution in the INS measurements on compound Fe_2Dy_2 (**5**).

For compound Fe_2Dy_2 (**5**) the INS measurements exhibit a rich spectrum, and nine magnetic peaks are clearly observed at 0.67 (1) meV (peak I), 1.03(1) meV (peak II), 1.21(1) meV (peak III), 1.37 (1) meV (peak IV), 1.71(1) meV (peak V), 1.93(3) meV (peak VI), 2.03(5) meV (peak VII), 2.49(2) meV (peak VIII), and 2.73(2) meV (peak IX). The intensities of these peaks decrease with increasing temperature, as shown in detail in Figure S8B. This, and the $S(Q,\omega)$ plot shown in Figure 5B, unambiguously identifies them as cold magnetic transitions. In these data a feature P4 is observed, which is spurious, as demonstrated in particular by the $S(Q,\omega)$ plot. The features observed at ~2.3 and ~3.0 meV clearly correspond to the features P4 and P5 observed for compound Al_2Dy_2 (**2**) and can thus safely be assigned as spurious. In the λ = 4.8 Å spectra, an additional very weak feature is observed at ~1.5 meV (labeled P1). The temperature dependence of its intensity and also the Q dependence do not rule out a magnetic origin. Based on its very weak intensity, it might be of extrinsic origin. Figure 5C presents the spectra recorded at T = 1.5 K in more detail. For this plot, the spectra were scaled with arbitrary factors such that the peak heights match within reason. The peak heights are slightly different in the λ = 4.25 and 4.8 Å data, which is partially due to the different experimental resolutions of 59 and 42 μeV, respectively, but mostly reflects the accuracy of the experiments. For this compound, high-resolution INS data were also recorded, with incident neutron wavelengths λ = 8.0 Å and transfer energies up to 0.8 meV, to investigate the low energy spectrum (Figure S10). The Stokes and anti-Stokes transitions corresponding to peak I are observed, but no further magnetic features at lower transfer energies can be detected in the energy range down to ~0.15 meV.

In Figure S9B, the spectra of compounds Al_2Dy_2 (**2**) and Fe_2Dy_2 (**5**) are shown for the neutron energy gain side. For compound Al_2Dy_2 (**2**), a broad feature that increases with temperature is observed at ca −1.5 meV, which represents the anti-Stokes feature corresponding to feature P2, which further corroborates the assignment as of phononic origin. In the data of compound Fe_2Dy_2 (**5**), the anti-Stokes peaks corresponding to the magnetic transitions I to IX can be identified, with the expected temperature dependence. For reasons similar to those for compound Al_2Er_2 (**1**), the magnetic data for compound Al_2Dy_2 (**2**) are not further discussed.

Magnetic models

The magnetism in the compounds Fe_2Y_2 (**3**), Fe_2Er_2 (**4**), and Fe_2Dy_2 (**5**) is modeled using the common spin Hamiltonian approach. Since Y^{III} is diamagnetic, compound Fe_2Y_2 (**3**) corresponds to an Fe^{III} dimer or a dimer of two spin 5/2 centers,

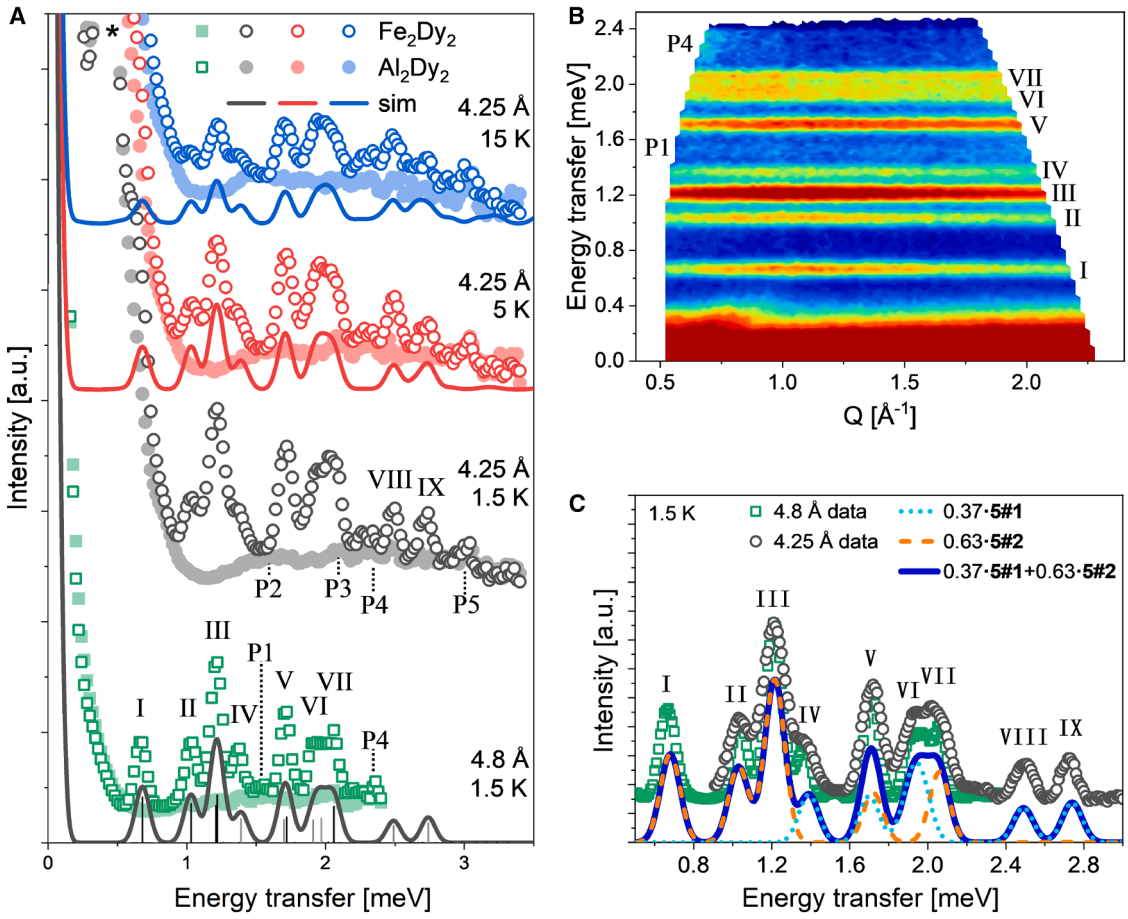

Figure 5. Experimental neutron energy loss INS spectra for Fe_2Dy_2 (5) and Al_2Dy_2 (2) and simulated curves

The data for Fe_2Dy_2 (**5**) and Al_2Dy_2 (**2**) are represented by open and solid symbols, respectively.

(A) INS spectra recorded with $\lambda = 4.8$ Å (squares) at $T = 1.5$ K (green) and with $\lambda = 4.25$ Å (circles) at $T = 1.5$ K (black), 5 K (red), and 15 K (blue). Datasets were shifted for clarity. Nine cold magnetic peaks, marked with Roman numbers, and five features, P1 to P5, are observed in the Fe_2Dy_2 (**5**) spectra. The Al_2Dy_2 (**2**) data show no magnetic features. The results of simulations are shown as solid lines with colors matching those of the associated experimental data. For $T = 1.5$ K, the simulated spectrum with assumed zero line width is also shown; gray bars represent the contribution of species **5#1** and black bars that of species **5#2**.

(B) $S(Q,\omega)$ plot for Fe_2Dy_2 (**5**) recorded at $T = 1.5$ K with $\lambda = 4.8$ Å.

(C) Zoom into the experimental $T = 1.5$ K spectrum for Fe_2Dy_2 (**5**) recorded with $\lambda = 4.8$ Å (green squares) and 4.25 Å (black circles). The simulated curves for species **5#1** and **5#2** and the combined sample Fe_2Dy_2 (**5**) are represented as dotted cyan, dashed orange, and solid blue lines, respectively.

In the plots, simulated curves were calculated using Equation 3 with the parameters given in the main text.

with a Heisenberg exchange interaction of strength J_{Fe-Fe}, single-ion magnetic anisotropy terms of second order described by tensors $\tilde{\boldsymbol{D}}_{Fe,i}$ ($i = 1, 2$), and a Zeeman term. Anisotropy tensors such as $\tilde{\boldsymbol{D}}_{Fe,i}$ are parameterized in this work by rotating a diagonal, traceless tensor $\boldsymbol{D}$, with the usual parameters D and E, by rotation matrices $\boldsymbol{R}$, as given in Equation 1. The rotation matrices are parametrized by the usual Euler angles θ, φ, and ψ.[70] The parameters D and E are chosen such that the local z' axis corresponds to the main anisotropy axis ($|E| \leq |D|/3$). The rotations are visualized in Figure 1B. In view of the inversion center of the investigated molecules, the main anisotropy axes of the two Fe^{III} ions can be assumed to be parallel to each other. In this work, the $-J$ notation is used for exchange couplings. The spin Hamiltonian for Fe_2Y_2 (**3**), thus, is as given in Equation 2. Symbols not discussed have their usual meaning:

$$\tilde{\boldsymbol{D}} = \boldsymbol{R}^T \boldsymbol{D} \boldsymbol{R} = \boldsymbol{R}^T \begin{pmatrix} -\frac{1}{3}D + E & 0 & 0 \\ 0 & -\frac{1}{3}D - E & 0 \\ 0 & 0 & \frac{2}{3}D \end{pmatrix} \boldsymbol{R}, \quad \text{(Equation 1)}$$

$$\hat{H}_1 = -J_{Fe-Fe}\hat{\boldsymbol{S}}_{Fe,1}\hat{\boldsymbol{S}}_{Fe,2} + \mu_B g_{Fe}\left(\hat{\boldsymbol{S}}_{Fe,1} + \hat{\boldsymbol{S}}_{Fe,2}\right)\boldsymbol{B} + \sum_{i=1,2} \hat{\boldsymbol{S}}_{Fe,i}\tilde{\boldsymbol{D}}_{Fe,i}\hat{\boldsymbol{S}}_{Fe,i}. \quad \text{(Equation 2)}$$

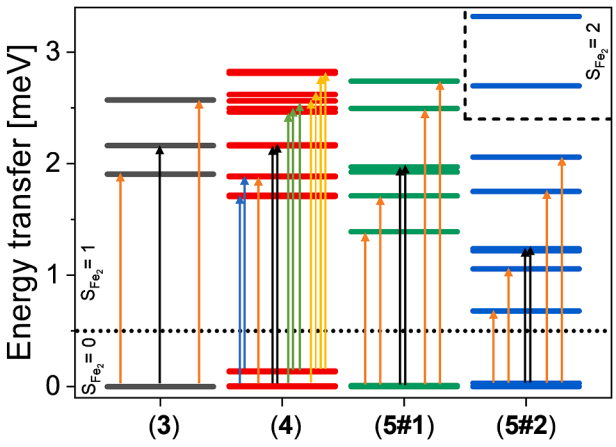

Figure 6. Simulated low-lying energy spectra for compounds Fe_2Y_2 (3), Fe_2Er_2 (4), and the two species in Fe_2Dy_2 (5) (5#1 and 5#2), from left to right

Levels originating from the S_{Fe_2} = 0 singlet spin state of the Fe_2 unit lie below the dotted horizontal line. Levels above that line originate from the S_{Fe_2} = 1 triplet spin state, except for **5#2**, for which the next higher levels originating from the S_{Fe_2} = 2 quintet spin state are also present at the higher energies (enclosed by dashed lines). The transitions observed in the INS experiments are indicated by vertical arrows. The fingerprint transitions discussed in the main text are represented by black arrows. The other transitions are indicated with orange arrows for compounds Fe_2Y_2 (**3**), **5#1**, and **5#2**, while for compound Fe_2Er_2 (**4**) the different transitions are in different colors for better clarity.

The magnetic models for compounds Fe_2Er_2 (**4**) and Fe_2Dy_2 (**5**) are based on the model for compound Fe_2Y_2 (**3**). In addition, exchange interactions between the lanthanide ions, J_{Ln-Ln}, and the Fe^{III} and lanthanide ions, J_{Fe-Ln}, are introduced. The lanthanide single-ion anisotropies are again modeled by second-order anisotropy tensors, $\tilde{\boldsymbol{D}}_{Ln}$, with respective D and E parameters and Euler angles. In the analysis of the data below, the relative angle between the main anisotropy axes of the Fe^{III} centers and the lanthanide centers will be of relevance and will be denoted as $\tilde{\theta}$. Second-order anisotropy tensors are sufficient for describing the lanthanide magnetism at low energies as relevant for the INS experiments and magnetization curves. For modeling the susceptibility curves, higher-order lanthanide anisotropy terms have in general to be introduced, but it was found that the effect of the ligand field splitting on the magnetic susceptibility can be modeled with sufficient accuracy by the magnitude of the D_{Ln} and E_{Ln} parameters, which thus can be viewed as lumped parameters (i.e., only the ratio $|E_{Ln}/D_{Ln}|$ is relevant for adjusting the low-energy behavior). The directions of the lanthanide main anisotropy axes can again be chosen to be parallel to each other, but are in general different from those of the Fe^{III} ions (see Figure 1B). The spin Hamiltonian for compounds Fe_2Er_2 (**4**) and Fe_2Dy_2 (**5**) is given in Equation 3:

$$\hat{H}_2 = \hat{H}_1 - J_{Ln-Ln}\hat{\boldsymbol{J}}_{Ln,1}\hat{\boldsymbol{J}}_{Ln,2} - J_{Fe-Ln}\sum_{i=1,2;j=1,2}\hat{\boldsymbol{S}}_{Fe,i}\hat{\boldsymbol{J}}_{Ln,j}$$

$$+ \mu_B g_{Ln}\left(\hat{\boldsymbol{J}}_{Ln,1} + \hat{\boldsymbol{J}}_{Ln,2}\right)\boldsymbol{B} + \sum_{i=1,2}\hat{\boldsymbol{J}}_{Ln,i}\tilde{\boldsymbol{D}}_{Ln,i}\hat{\boldsymbol{J}}_{Ln,i}. \quad \text{(Equation 3)}$$

In order to avoid confusion with exchange coupling constants, operators are indicated by a hat. Dipolar magnetic interactions, especially with lanthanide ions, should in general be included as well. However, we have checked that they do not introduce appreciable effects other than slightly changing the values of some parameters (*vide infra*), in accord with expectation.

The INS scattering intensity of powder samples was simulated using the formula given in Waldmann and Güdel[71,72] In the simulation of the magnetic susceptibilities, a correction χ_0, to account for experimental inaccuracies in the diamagnetic correction, and an intermolecular exchange interaction, modeled via a Curie-Weiss constant θ_C,[27] were in addition considered as necessary. For each compound, one set of best-fit parameters, which reproduces all experimental data (INS, magnetization, and susceptibility) for that compound, was determined by stepwise combination of least-squares fits and extensive grid calculations.

The effect of the orientations of the anisotropy axes in the model, i.e., the rotation matrices in the $\tilde{\boldsymbol{D}}_{Fe}$ and $\tilde{\boldsymbol{D}}_{Ln}$ tensors, on the considered experimental observables warrants a comment. The assumed spin Hamiltonians do not explicitly depend on the coordinates of the metal centers, and the calculated energies and wave functions thus do not depend on a global rotation of the anisotropy tensors with respect to the molecular structure ("global" meaning a rotation of all tensors by the same Euler angles). Therefore, one cannot determine the absolute orientations of the anisotropy axes with respect to the molecule from the INS transition energies and powder magnetization and susceptibility curves but only the relative orientations of anisotropy axes with respect to each other. The situation is, however, markedly different for the INS intensities, since the INS scattering formula involves interference terms, i.e., terms that explicitly depend on the coordinates of the metal centers.[40,73] Therefore, the INS intensities can depend on the absolute orientations of the anisotropy axes, providing a potential path to reveal such information from INS, even on powder samples. This is exemplarily demonstrated for compound Fe_2Y_2 (**3**) in Figure S6C.

The Fe^{III}-Fe^{III} interactions will be determined to be antiferromagnetic, as expected from the magnetic data of Fe_2Y_2 (**3**), and dominate the structure of the energy spectra in the relevant energy window of a few meV. The general structure of the energy spectra, then, is as follows. For compound Fe_2Y_2 (**3**), a singlet ground state, S_{Fe_2} = 0, is obtained, with three excited levels originating from the excited triplet S_{Fe_2} = 1 and the zero-field splitting due to the Fe^{III} anisotropy terms (S_{Fe_2} refers to the spin state of the Fe_2 unit). The energy spectrum is sketched in Figure 6. Ignoring the lanthanide rhombic terms in the spin Hamiltonian (Equation 3), the states in the compounds Fe_2Er_2 (**4**) and Fe_2Dy_2 (**5**) can be described as $|S_{Fe_2}, m_{J,Ln,1}, m_{J,Ln,2}\rangle$, where $m_{J,Ln}$ refers to the magnetic quantum numbers of the ground Kramers doublets of the two lanthanide ions in the cluster (a further quantum number required to completely specify the spin state of the Fe_2 unit is dropped for brevity). The lanthanide magnetic quantum numbers can assume the values $m_{J,Ln} = \pm M_J$ (M_J will be specified later). Therefore, disregarding the 3d-4f and 4f-4f interactions, the ground levels of the cluster consist of the 4 states $|0, \pm M_J, \pm M_J\rangle$ and a set of 12 higher-lying states $|1, \pm M_J, \pm M_J\rangle$, which energy-wise are located around the Fe_2 singlet-triplet excitation energy, or $|J_{Fe-Fe}|$ in fact. The 3d-4f

and 4f-4f interactions induce splittings, but a 2-fold degeneracy remains. The energy spectrum is then characterized by two slightly separated doublets at low energies and a set of six excited doublets at higher energies. The lanthanide rhombic terms in Equation 3 shift the levels in energy and induce further splittings, lifting the 2-fold degeneracy, which is, however, comparatively weak. As a result, a characteristic pattern of six or more levels at energies of around $|J_{Fe-Fe}|$ emerges in the accessible energy window probed in the present INS experiments, as sketched in Figure 6. The lanthanide ligand-field parameter D_{Ln} can be expected to be large, larger than all other terms. As mentioned before, the low-energy spectrum, as relevant in the INS and magnetization experiments, is therefore governed by the ratio $|E_{Ln}/D_{Ln}|$ but is largely independent of the absolute values of D_{Ln} and E_{Ln}.

Modeling of Fe_2Y_2

For compound Fe_2Y_2 (**3**), the parameters $J_{Fe-Fe} = -25.4(1)$ K, $D_{Fe} = 0.98(4)$ K, $|E_{Fe}| = 0.23(3)$ K, $\theta_{Fe} = 70(20)^\circ$, and $\varphi_{Fe} = 0(20)^\circ$ were determined using Equation 2. The simulated INS curves are shown in Figures 2 and S6A. The simulations reproduce the experimental data very well. Noteworthily, the simulated intensities of the observed INS peaks depend on the absolute orientations of the Fe^{III} anisotropy axes, allowing us to determine both the polar and the azimuthal angles θ_{Fe} and φ_{Fe} with significance (though not very accurately as indicated by the estimated standard deviations). In the case of compound Fe_2Y_2 (**3**), a rotation of $\boldsymbol{D}_{Fe}$ corresponds to a global rotation and therefore does not change the energy spectrum, nor the peak positions, but does affect the peak intensities. For this compound, the sign of E_{Fe} cannot be determined from the powder data. Also, note that the simulated curves are identical for θ_{Fe} and $180^\circ - \theta_{Fe}$; i.e., $\theta_{Fe} = 110(20)^\circ$ is an equally valid solution. The calculated energy spectrum is plotted in Figure 6, which also indicates the observed INS transitions. Fits to the magnetic susceptibility (Figure 2) yielded a coupling constant of $J_{Fe-Fe} = -21.2(1)$ K, slightly smaller than the INS value but in reasonable agreement, given that INS probes the low-energy sector, while magnetic susceptibility probes the complete energy spectrum.

Modeling of Fe_2Er_2

For compound Fe_2Er_2 (**4**), the parameters $J_{Fe-Fe} = -23.4(1)$ K, $D_{Fe} = 0.98(5)$ K, $E_{Fe} = 0.26(4)$ K, $J_{Fe-Er} = -0.39(5)$ K, $J_{Er-Er} = -0.015(5)$ K, $D_{Er} = 60(10)$ K, $E_{Er} = -1.5(5)$ K, and $\tilde{\theta} = 59(5)^\circ$ were determined using Equation 3. In the modeling of the susceptibility, a contribution $\chi_0 = 0.005$ emu K mol^{-1}, was included, as well as a Curie-Weiss constant of $\theta_C = -0.35$ K. The simulated INS curves are shown in Figures 3A, S8A, and S9A. The five experimentally observed transitions, I–V, are well reproduced. In order to reproduce the INS and magnetization data, a non-zero lanthanide rhombic term, E_{Er}, was found to be required. While the simulated peak positions depend on all parameters, often in subtle ways, it was found that especially the energy of peak IV depends significantly on the relative angle $\tilde{\theta}$, which thus could be determined from the experiment with good significance. The simulated peak intensities also depend on all parameters, often in subtle ways. However, here, it was found that especially the intensity of peak II is sensitive to the absolute orientations of the Fe^{III} and Er^{III} anisotropy axes. Information on the absolute orientations can thus be deduced from the data, but the data are not sufficient to pin down all six Euler angles in the model (Equation 3). With the relative angle $\tilde{\theta}$ fixed, five free parameters are remaining. The directions of the lanthanide main anisotropy axis in relation to the Fe^{III} main anisotropy axis, which are consistent with the determined relative angle $\tilde{\theta}$, thus span a cone as indicated in Figure 1B. The peak intensities do depend on the five undetermined free parameters, but the variations were found to be too small to be determined from the experiments. In the simulation, they were thus set arbitrarily (we used $\theta_{Er} = 60^\circ$, $\varphi_{Er} = 120^\circ$, $\alpha_{Er} = 80^\circ$, $\theta_{Fe} = 83^\circ$, $\varphi_{Fe} = 178^\circ$, and $\alpha_{Fe} = 149^\circ$). The simulated χT and $M(B)$ curves are shown in Figure 3C as solid lines. As evident from the figures, all experimental data are well reproduced by the one parameter set given in the above.

The calculated energy spectrum is plotted in Figure 6, with the observed INS transitions indicated by arrows. The transition energies of peaks II and III are essentially identical to those of peaks I and II in compound Fe_2Y_2 (**3**). The higher of the two, i.e., peak III in Fe_2Er_2 (**4**) or peak II in Fe_2Y_2 (**3**), was found to be relatively insensitive to variations in the model parameters besides J_{Fe-Fe} and thus can be regarded as a fingerprint of the underlying triplet state of the antiferromagnetically coupled Fe_2 unit. Peak IV is made up of several close-lying transitions not resolved in the experiment.

Modeling of Fe_2Dy_2

The modeling of the data for compound Fe_2Dy_2 (**5**) was more complicated than for the other compounds. Intense efforts to model the data, especially the INS data, assuming a single species in the compound failed. As discussed before, with reasonable parameter values a characteristic energy spectrum is obtained from Equation 3. It was found impossible to produce INS spectra exhibiting nine peaks as widely spread out in energy as observed in the experiment and simultaneously be consistent with the neutron energy gain spectra and the magnetization curves. One possibility for creating sufficiently many peaks would be to assume a very-low-lying ligand field level for the Dy^{III} ions, but in such models neither the temperature dependencies of the INS intensities nor the magnetization curves nor the susceptibility could be reproduced within reason. Another possibility would be to assume a small Fe^{III}-Fe^{III} exchange coupling constant such that the levels associated with the $S_{Fe_2} = 2$ quintet spin state move into the experimental window. Such a model in fact can explain the indications of a level crossing observed in the magnetization curves (*vide infra*). However, the INS transitions related to the quintet spin states would be hot transitions and thus not be observed at the lowest temperatures, in marked contrast to the experiment. In addition, models were considered in which the assumed inversion center was removed, or broken exchange coupling paths were assumed.

It eventually was concluded that the INS sample consisted of two species, denoted as **5#1** and **5#2** in the following, and that the observed data are the result of the combined contributions from the two. A retrospective careful analysis of the sample by PXRD indeed confirmed that it consisted of a mixture of **5-A** and **5-B**, as described earlier (the association of species **5#1**

and **5#2** with polymorphs A and B is not obvious from the INS data; hence, the distinction in the notation).

Equipped with the experience and insights from the analysis of compound Fe_2Er_2 (**4**), it is then straightforward to infer from the INS data in which parameter the two species differ most. Each species is expected to contribute a characteristic pattern of INS transitions, with a fingerprint transition for each of them. The observed peaks III and V are readily identified as the fingerprints, which strongly suggests that the key differences between the two species are significantly different Fe^{III}-Fe^{III} exchange couplings. Since the energy of peak VI is similar to the energies of the fingerprint transitions observed in compounds Fe_2Y_2 (**3**) and Fe_2Er_2 (**4**), it can be concluded that for species **5#1**, J_{Fe-Fe} is of similar value (ca −23 K). Peak III is ca. 40% lower in energy, which allows one to conclude that in species **5#2**, J_{Fe-Fe} is correspondingly smaller (suggesting ca −14 K).

Precise modeling yielded for species **5#1** the parameter set J_{Fe-Fe} = −23.2(2) K, D_{Fe} = 1.24(3) K, E_{Fe} = −0.19(3) K, J_{Fe-Dy} = −0.42(1) K, J_{Dy-Dy} = 0.0010(5) K, D_{Dy} = −15(5) K, and $\tilde{\theta}$ = 52(5)° and for species **5#2** the set J_{Fe-Fe} = −14.8(2) K, D_{Fe} = 1.09(3) K, E_{Fe} = −0.16(3) K, J_{Fe-Dy} = −0.46(1) K, J_{Dy-Dy} = 0.003(1) K, D_{Dy} = −15(5) K, and $\tilde{\theta}$ = 58(5)°. In the modeling of the susceptibility, a diamagnetic correction χ_0 = 0.008 emu K mol^{-1} and a Curie-Weiss constant θ_C = −0.25 K were included. The composition of the sample was obtained as 37% of **5#1** and 67% of **5#2**.

The simulated INS spectra are shown in Figure 5A and, for one spectrum in detail, in Figure 5C. The temperature dependencies and the neutron energy gain spectra are presented in Figures S8B, S9B, and S10. The agreement with experimental data is very good. In Figure 5C the contributions from the two species are also shown (dash and dotted lines).

Figure 4A displays the simulated χT curves for Fe_2Dy_2 (**5**) and the species **5#1** and **5#2**. Figure 4B presents the simulated *M(B)* curve for Fe_2Dy_2 (**5**). The experimental data are reasonably well reproduced. The magnetization at high fields is slightly too small in the simulation. However, the intersection at ∼4.1 T (marked by black arrows) is reproduced well, which provides strong evidence that the model catches the essentials well.

The simulated energy spectra for both species are shown in Figure 6, with the observed INS transition indicated as arrows. For each species the characteristic energy pattern discussed before is obtained but with the energies moved to lower values for species **5#2**, according to the ∼40% smaller exchange coupling J_{Fe-Fe}. Therefore, for species **5#2** a field-induced level crossing is expected to occur at a substantially smaller field than for species **5#1**. The intersection in the magnetization, indicative of a field-induced level crossing, does in fact stem from the contribution of species **5#2** to the magnetization. For species **5#2** the high-lying levels originating from the S_{Fe_2} = 2 quintet spin state of the Fe_2 unit fall into the experimental window. They are not detected in the INS experiments because the associated transitions are hot and the transition spectrum is spread out.

DISCUSSION

The presented results imply a number of interesting discussion points. First, it is interesting to note that for compounds Fe_2Er_2 (**4**) and Fe_2Dy_2 (**5**), the intensity of the INS peaks observed in this work mostly stems from the 3d metal ions, while the 4f ions essentially do not contribute. This may appear counterintuitive, given the large angular momentum and thus large expected magnetic scattering strength of the Er^{III} and Dy^{III} ions. In simulations this can be demonstrated by setting the lanthanide g_{Ln} factors to zero, which simulates a non-existing interaction between the neutrons and the lanthanide ions, canceling this scattering mechanism. Simulated spectra for $g_{Ln} = g_J$ and $g_{Ln} = 0$ are compared to each other in Figure S11 for both compounds Fe_2Er_2 (**4**) and Fe_2Dy_2 (**5**). At low transition energies the spectra are identical, showing that, here, all intensity is indeed due only to the scattering by the 3d metal ions. At higher transition energies the lanthanide ligand-field excitations come into play, and the lanthanide ions contribute to the scattering intensity (and may even dominate). This finding is explained by the fact that the transitions observed in this work involve a $\Delta S_{Fe_2} = \pm 1$ transition located on the Fe_2 unit, leaving the lanthanide ion states untouched. The 3d-4f SMMs can thus indeed be more amenable to detailed spectroscopic studies. While not through the INS intensities, the presence of the lanthanide ions affects the energy spectrum and thus the INS peak positions, through which their properties become observable in the above experiments. The described mechanism is not limited to the compounds studied in this work, or to 3d-4f butterfly compounds, but establishes a more general principle applicable to a large variety of 3d-4f molecular clusters.

In the model for compounds Fe_2Er_2 (**4**) and Fe_2Dy_2 (**5**), Equation 3, the lanthanide ligand field is described by a second-order anisotropy, and $D_{Er} > 0$ and $D_{Dy} < 0$ were found. Accordingly, the ground Kramers doublet $m_{J,Ln} = \pm M_J$ in the models corresponds to M_J = 1/2 for Er^{III} and M_J = 15/2 for Dy^{III}. It is well known, however, that in 4f-containing SMMs the ground Kramers doublet often is not the minimally/maximally polarized state for Er^{III}/Dy^{III}.[29,74–76] For compound Fe_2Dy_2 (**5**) the assumption of M_J = 15/2 does, however, not introduce essential inaccuracies in the modeling, since the relevant aspect is the strong uniaxial nature of the lanthanide states in the cluster state $|S_{Fe_2}, m_{J,Ln,1}, m_{J,Ln,2}\rangle$ (meaning that $\langle M_J|\hat{\boldsymbol{J}}_{Ln}|-M_J\rangle = 0$ holds). The model parameters may come out slightly differently when assuming a different (reasonable) ground Kramers doublet, but the model will work equally well, and key conclusions, especially concerning the Fe^{III}-Fe^{III} coupling and the orientations of the anisotropy axes, are robust. For compound Fe_2Er_2 (**4**), the situation is less obvious, since here, $\langle M_J|\hat{\boldsymbol{J}}_{Ln}|-M_J\rangle \neq 0$ for M_J = 1/2. However, here, too, numerical tests assuming, e.g., M_J = 3/2 or 5/2 showed that, while for instance the value of the parameter E_{Er} comes out somewhat differently depending on the assumed ground Kramers doublet, the key conclusions concerning the orientations of the anisotropy axes are robust. Noteworthily, if one assumes a small M_J for Dy^{III}/large M_J for Er^{III}, then the experimental INS data cannot be reasonably reproduced. That is, from the experiment it can be concluded that the ground Kramers doublet of Dy^{III} in Fe_2Dy_2 (**5**) is maximally or nearly maximally polarized (M_J equal or close to 15/2) and that of Er^{III} in Fe_2Er_2 (**4**) is minimally or nearly minimally polarized (M_J equal or close to 1/2).

The opposite signs of D_{Er} and D_{Dy} nicely correlate with the opposite signs of the second-order Stevens factors for Er^{III} and

Dy^{III} (α_{ErIII} = 4/1,575 and α_{DyIII} = −2/315[77]). For structurally related complexes, the ligand field parameters are expected to be transferable and scale according to the Stevens factors.[78–80] In other terms, the lanthanide ligand field environment in compounds Fe_2Er_2 (**4**) and Fe_2Dy_2 (**5**) appears to stabilize the oblate lanthanide states.[18,81]

Our study also yielded values for the 3d-4f and 4f-4f interactions J_{Fe-Ln} and J_{Ln-Ln}. The coupling constant J_{Fe-Ln} was found to have a relatively large effect on the simulated energy spectrum and thus could be relatively well determined from the INS spectra. In the model, dipole-dipole interactions were not included. Explicitly including them yielded J_{Fe-Ln} values that were different by at most 0.02 K, which is within experimental uncertainty. The findings for J_{Fe-Ln} should thus be considered scientifically significant and to represent the exchange interactions. Similar J_{Fe-Ln} values of ca −0.45 K were determined for Fe_2Er_2 (**4**), **5#1**, and **5#2**. These are expressed in the *J* multiplet, but exchange involving 4f ions is often considered to be better described as interaction between the spin components.[77] Then, since $\widehat{\boldsymbol{S}} = (g_J - 1)\widehat{\boldsymbol{J}}$ in a *J* multiplet, the 3d-4f exchange constants should be multiplied by a factor, $(g_J - 1)^{-1}$, to yield the coupling strengths with respect to spin, or factors 5 and 3 for Er^{III} and Dy^{III}, respectively, yielding ca −2.1 K and ca −1.5 K. It thus appears that de Gennes factor-like scaling is not well obeyed here.[77] The 4f-4f interaction parameter, in contrast, was found to have negligible effect on the simulated energy spectrum but has a characteristic effect on the INS intensities. However, the determined values are very small, in the range of few millikelvins, and comparable in magnitude to the dipole-dipole interaction. Even though values were obtained with statistical significance, this parameter should thus be considered a lumped parameter, and the reported values for J_{Ln-Ln} should not be given scientific significance.

A particularly interesting observation is the substantially different Fe^{III}-Fe^{III} exchange coupling constants in the Fe_2Dy_2 species **5#1** and **5#2**, determined to ca −23 K and −15 K, respectively. The spectroscopic INS data are unambiguous in this point. Given that J_{Fe-Fe} is similar for the samples of Fe_2Y_2 (**3**) and Fe_2Er_2 (**4**) and that both compounds were present as polymorph B, it appears reasonable to assign species **5#1**, which exhibits a J_{Fe-Fe} similar to that of Fe_2Y_2 (**3**) and Fe_2Er_2 (**4**), also to polymorph B. Species **5#2** would then be associated with polymorph A. The geometry of the Fe-O-Fe exchange paths is essentially identical in all the Fe_2Ln_2 structures, and magneto-structural correlations[82] thus predict essentially identical J_{Fe-Fe} coupling strengths (see Table S2). The observation of a significantly different (smaller) Fe^{III}-Fe^{III} exchange coupling in species **5#2** could indicate an unexpected modulation of the exchange coupling by the different solvent molecules (acetonitrile or methanol) accepting the H bonds from the (μ_3-OH) bridges. Partly because SMM behavior is a molecular effect, it has become traditional to consider only the magnetic molecule itself and not counterions and, more particularly, neutral solvent molecules in the crystal lattice. However, it has been shown that, e.g., changes in the crystal lattice symmetry can have a significant effect on 4f ligand fields.[83] The results presented here appear to suggest that one should go further. The molecular structures of the Fe_2Dy_2 species **5#1** and **5#2** do not differ significantly; the main difference between their two crystal polymorphs is supramolecular, concerning the lattice solvent molecules that accept the hydrogen bonds from the (μ_3-OH) bridges. Such supramolecular modulation of intramolecular magnetic exchange interactions is an unexpected but interesting result of this study.

The main result of this work concerns identifying the orientations of the anisotropy axes. For compound Fe_2Y_2 (**3**), it was shown that the careful analysis of the INS intensities in exchange-coupled dimers, here, the single-triplet transitions, can provide substantial information on the single-ion anisotropy orientations. To the best of our knowledge, this has not been previously exploited. The main anisotropy axis (local *z* direction) was found to be directed along the connection line between the two Fe^{III} ions, with a tilt of ca. 20° away from the plane of the molecule (*xy* plane). The single-ion anisotropy was found to be substantially rhombic, however ($|E_{Fe}/D_{Fe}|$ = 0.23), and the anisotropy is thus not well described by a main anisotropy axis.

For compounds Fe_2Er_2 (**4**) and Fe_2Dy_2 (**5**), the relative angle between the Fe^{III} and the Ln^{III} anisotropy axes, $\tilde{\theta}$, could be determined fairly accurately. For the two species in compound Fe_2Dy_2 (**5**) (**5#1** and **5#2**), these angles were found to be 52(5)° and 58 (5)°, respectively. For compound Fe_2Dy_2 (**5**), a recent *ab initio* calculation yielded Fe^{III} main anisotropy axes, which are directed essentially along the Fe^{III}-Fe^{III} connection line, and Dy^{III} main anisotropy axes, which lie essentially in the molecule plane (*xy* plane), with the Fe^{III} and Dy^{III} main anisotropy axes subtending an angle of 73°.[60] This calculated relative angle is significantly larger than our result and quantitatively not consistent with the experimental data. If one disregards this discrepancy, the qualitative overall picture found from the *ab initio* calculations could be consistent with the experimental data: the experiments did not permit us to determine the absolute directions of the Fe^{III} main anisotropy axes in Fe_2Dy_2 (**5**), but for the analog Fe_2Y_2 (**3**), the Fe^{III} main axes were found to be essentially directed as calculated for Fe_2Dy_2 (**5**) by *ab initio* theory. If one assumes that the Fe^{III} main axes are essentially along the Fe^{III}-Fe^{III} connection line also in Fe_2Dy_2 (**5**), then the Dy^{III} main axes, which are essentially in-plane with angles of ∼55° to the Fe^{III} main axes, would indeed be consistent with the experimental data. It needs to be emphasized, however, that our experimental data do not provide a unique solution for the orientations of the anisotropy axes and that, therefore, very different theoretical results can also be consistent with the data. For compound Fe_2Er_2 (**4**), results from *ab initio* theory are not available.

In this work, a systematic spectroscopic INS study on five members of an isostructural family of 3d-4f molecular $M^{III}_2Ln^{III}_2$ complexes with a butterfly structure has been presented. Despite the samples being non-deuterated, the experimental INS data are of high quality in terms of the statistics of the magnetic signal (this is demonstrated, e.g., by the fact that $S(Q,\omega)$ plots with significant resolution were obtained) as well as in terms of the number of observed magnetic peaks and hence information content. While these attributes are common for INS studies on 3d molecular clusters, they are unprecedented for INS studies on polynuclear 4f-containing complexes.[47,48,51,52] As shown and discussed in this work, this can be related to the advantages provided by 3d-4f molecular complexes with regard to INS, in that they mitigate some of the challenges in pure 4f

systems. This suggests a sustainable approach to targeting these data without the need for expensive deuteration and/or rare isotopes.

Precise magnetic models, formulated in terms of spin Hamiltonians operating in the total angular momentum/spin space, could be determined. It was possible to describe accurately the low-energy excitations (up to a few meV) in the target compounds Fe_2Er_2 (**4**) and Fe_2Dy_2 (**5**). The spectroscopic data recorded on the analogous compounds in which magnetic centers were substituted by diamagnetic ions proved crucial for assigning the magnetic features in the INS spectra of the target compounds.

A major result of the study is the determination of the orientation of the local magnetic anisotropy axes. For Fe_2Y_2 (**3**), it was found that the Fe^{III} main anisotropy axis is oriented in the direction of the vector between the two Fe^{III} centers, with a tilt of ~20° out of the plane spanned by the four metal centers. For Fe_2Er_2 (**4**) and Fe_2Dy_2 (**5**), the relative angles between the main anisotropy axes of the Ln^{III} and Fe^{III} centers were determined to be ~59° for Fe_2Er_2 (**4**) and ~52° or ~58° for Fe_2Dy_2 (**5**) (where the angle depends on the polymorph).

An unexpected finding is the significant differences in the Fe^{III}-Fe^{III} exchange couplings in "polymorph A" and "polymorph B" of the Fe_2Dy_2 cluster. Our study thus provides evidence for a previously unsuspected second sphere effect on the Fe^{III}-Fe^{III} exchange coupling in this class of compounds, indicating that neutral lattice solvent molecules may modulate intramolecular exchange couplings.

The determination of the single-ion anisotropy axes in polynuclear clusters represents an experimental challenge. In homonuclear clusters such as Fe_2Y_2 (**3**), in which the directions of the anisotropy axes are parallel for all spin sites (the Fe^{III} ions in this case), a favorable crystal structure is also required. These directions can be determined using magnetic measurements such as magnetic susceptibility, magnetization curves, and torque magnetometry on single crystals.[33,79,84] If the condition of parallel anisotropy axes is not met, physical methods allowing access to local information need to be invoked. The requirement for single-crystal measurements for INS studies represents a major hurdle. Whereas INS spectra recorded on powder samples provide less information than single crystal studies, our study has shown that valuable information on the orientations can be obtained.

The basis for the comparatively strong INS signals in the studied compounds, which made the experiments on non-deuterated samples possible, was revealed. It was, in particular, demonstrated that it is not limited to the class of butterfly complexes but is applicable to a wider range of compounds. The implications are far reaching, since this opens a general experimental path for high-quality INS experiments precluding the need for deuteration, which is not only cost effective and environmentally friendly but also scientifically exciting.

METHODS

Compounds **1**–**5** were synthesized as described previously.[56,57] The crystal phase(s) present in each sample was checked by PXRD (more experimental details are given in the supplemental information).

For the INS studies, non-deuterated material was finely ground, yielding a polycrystalline powder, and filled into double-walled hollow aluminum cans. INS spectra of the two Dy^{III}-containing compounds, Al_2Dy_2 (**2**) and Fe_2Dy_2 (**5**), were recorded on the spectrometer IN5[85,86]; for the three compounds Al_2Er_2 (**1**), Fe_2Y_2 (**3**), and Fe_2Er_2 (**4**), data were taken on the spectrometer IN6-SHARP (CRG operated by LLB-Saclay at ILL).[87,88] Both instruments are direct time-of-flight spectrometers at the ILL. The data were corrected for detector efficiency via a vanadium standard, and background correction was done via an empty can measurement. The data presented correspond to the sum of all momentum transfers Q, except in the $S(Q,\omega)$ plots (energy transfer ω vs. momentum transfer Q). Positive energies correspond to neutron energy loss (Stokes/anti-Stokes lines appear at positive/negative energy transfer). The experimental error bars are generally smaller than the symbol sizes in the plots.

Magnetization as a function of applied magnetic field $M(B)$ and temperature-dependent magnetic susceptibility $\chi(T)$ were collected using an MPMS SQUID VSM from Quantum Design. The $\chi(T)$ curves were obtained from measurements at an applied field of $B = 0.1$ T. The samples were prepared by taking a part of the INS sample and mixing with eicosane to prevent alignment of the microcrystallites in the applied magnetic field. All data were corrected for the diamagnetic contributions from the sample holder and the eicosane. The full details of the measurement procedure are described in the supplemental information.

In the data plots, the experimental data for compounds Al_2Er_2 (**1**) and Al_2Dy_2 (**2**) are generally represented by solid symbols and for compounds Fe_2Y_2 (**3**), Fe_2Er_2 (**4**), and Fe_2Dy_2 (**5**) by open symbols. Simulated data are generally represented by lines.

Further details regarding the methods can be found in the supplemental methods.

RESOURCE AVAILABILITY

Lead contact

Further information is available upon reasonable request from the lead contact, Oliver Waldmann (oliver.waldmann@physik.uni-freiburg.de).

Materials availability

This study did not generate new reagents.

Data and code availability

- Full crystallographic data and details of the structural determinations for the structures in this paper have been deposited with the Cambridge Crystallographic Data Centre. The CCDC deposition numbers of **1**, **2**, **4**, **5**, and the doped $Al_2(Y/Dy)_2$ form of **2** are 1821361, 1428525, 1821360, 1428524, and 1880460, respectively, and are also given in Table S1. Copies of the data can be obtained, free of charge, from https://www.ccdc.cam.ac.uk/structures/. The experimental INS data are available at https://doi.org/10.5291/ILL-DATA.4-06-11; see also Waldmann.[72]
- This study did not generate original code.
- Information required to reanalyze the data is reported in this paper. Further information is available from the corresponding authors upon reasonable request.

ACKNOWLEDGMENTS

This study was partially funded by the Deutsche Forschungsgemeinschaft CRC 1573 "4f for Future," the Helmholtz POF MSE, and the German Ministry of Education and Research (network project EPR-Solar 03SF0328E).

AUTHOR CONTRIBUTIONS

Y.P. and T.R. prepared the samples. J.M., Y.P., and O.W. performed the INS experiments, assisted by J.O., Q.B., and J.-M.Z. S.S., T.R., and Y.F.S. performed the magnetic measurements. J.M. performed the data analysis, and J.M. and O.W. developed the models. The paper was written by J.M., J.B., C.E.A., A.K.P., and O.W. All authors discussed the results and commented on the manuscript.

DECLARATION OF INTERESTS

The authors declare no competing interests.

SUPPLEMENTAL INFORMATION

Supplemental information can be found online at https://doi.org/10.1016/j.xcrp.2025.102848.

Received: December 2, 2024
Revised: June 25, 2025
Accepted: August 25, 2025
Published: September 22, 2025

REFERENCES

1. Sessoli, R., Gatteschi, D., Caneschi, A., and Novak, M.A. (1993). Magnetic bistability in a metal-ion cluster. Nature *365*, 141–143.
2. Sessoli, R., Tsai, H.L., Schake, A.R., Wang, S., Vincent, J.B., Folting, K., Gatteschi, D., Christou, G., and Hendrickson, D.N. (1993). High-spin molecules: [Mn12O12(O2CR)16(H2O)4]. J. Am. Chem. Soc. *115*, 1804–1816.
3. Christou, G., Gatteschi, D., Hendrickson, D.N., and Sessoli, R. (2000). Single-Molecule Magnets. MRS Bull. *25*, 66–71.
4. Luis, F., Repollés, A., Martínez-Pérez, M.J., Aguilà, D., Roubeau, O., Zueco, D., Alonso, P.J., Evangelisti, M., Camón, A., Sesé, J., et al. (2011). Molecular prototypes for spin-based CNOT and SWAP quantum gates. Phys. Rev. Lett. *107*, 117203.
5. Bernot, K., Daiguebonne, C., Calvez, G., Suffren, Y., and Guillou, O. (2021). A Journey in Lanthanide Coordination Chemistry: From Evaporable Dimers to Magnetic Materials and Luminescent Devices. Acc. Chem. Res. *54*, 427–440.
6. Gabarró-Riera, G., Aromí, G., and Sañudo, E.C. (2023). Magnetic molecules on surfaces: SMMs and beyond. Coord. Chem. Rev. *475*, 214858.
7. Chiesa, A., Santini, P., Garlatti, E., Luis, F., and Carretta, S. (2024). Molecular nanomagnets: a viable path toward quantum information processing? Rep. Prog. Phys. *87*, 1361.
8. Chicco, S., Allodi, G., Chiesa, A., Garlatti, E., Buch, C.D., Santini, P., de Renzi, R., Piligkos, S., and Carretta, S. (2024). Proof-of-Concept Quantum Simulator Based on Molecular Spin Qudits. J. Am. Chem. Soc. *146*, 1053–1061.
9. Leuenberger, M.N., and Loss, D. (2001). Quantum computing in molecular magnets. Nature *410*, 789–793.
10. Moreno-Pineda, E., Godfrin, C., Balestro, F., Wernsdorfer, W., and Ruben, M. (2018). Molecular spin qudits for quantum algorithms. Chem. Soc. Rev. *47*, 501–513.
11. Gaita-Ariño, A., Luis, F., Hill, S., and Coronado, E. (2019). Molecular spins for quantum computation. Nat. Chem. *11*, 301–309.
12. Biard, H., Moreno-Pineda, E., Ruben, M., Bonet, E., Wernsdorfer, W., and Balestro, F. (2021). Increasing the Hilbert space dimension using a single coupled molecular spin. Nat. Commun. *12*, 4443.
13. Ruiz, E., Cirera, J., Cano, J., Alvarez, S., Loose, C., and Kortus, J. (2008). Can large magnetic anisotropy and high spin really coexist? Chem. Commun. *1*, 52–54.
14. Waldmann, O. (2007). A criterion for the anisotropy barrier in single-molecule magnets. Inorg. Chem. *46*, 10035–10037.
15. Zabala-Lekuona, A., Seco, J.M., and Colacio, E. (2021). Single-Molecule Magnets: From Mn12-ac to dysprosium metallocenes, a travel in time. Coord. Chem. Rev. *441*, 213984.
16. Bernot, K. (2023). Get under the Umbrella: A Comprehensive Gateway for Researchers on Lanthanide-Based Single-Molecule Magnets. Eur. J. Inorg. Chem. *26*, e202300336.
17. Benelli, C., and Gatteschi, D. (2015). Introduction to Molecular Magnetism. From Transition Metals to Lanthanides (Wiley-VCH).
18. Rinehart, J.D., and Long, J.R. (2011). Exploiting single-ion anisotropy in the design of f-element single-molecule magnets. Chem. Sci. *2*, 2078.
19. Sessoli, R., and Powell, A.K. (2009). Strategies towards single molecule magnets based on lanthanide ions. Coord. Chem. Rev. *253*, 2328–2341.
20. Ishikawa, N. (2007). Single molecule magnet with single lanthanide ion. Polyhedron *26*, 2147–2153.
21. Guo, F.-S., Day, B.M., Chen, Y.-C., Tong, M.-L., Mansikkamäki, A., and Layfield, R.A. (2018). Magnetic hysteresis up to 80 kelvin in a dysprosium metallocene single-molecule magnet. Science *362*, 1400–1403.
22. Goodwin, C.A.P., Ortu, F., Reta, D., Chilton, N.F., and Mills, D.P. (2017). Molecular magnetic hysteresis at 60 kelvin in dysprosocenium. Nature *548*, 439–442.
23. Randall McClain, K., Gould, C.A., Chakarawet, K., Teat, S.J., Groshens, T.J., Long, J.R., and Harvey, B.G. (2018). High-temperature magnetic blocking and magneto-structural correlations in a series of dysprosium (iii) metallocenium single-molecule magnets. Chem. Sci. *9*, 8492–8503.
24. Gould, C.A., McClain, K.R., Reta, D., Kragskow, J.G.C., Marchiori, D.A., Lachman, E., Choi, E.-S., Analytis, J.G., Britt, R.D., Chilton, N.F., et al. (2022). Ultrahard magnetism from mixed-valence dilanthanide complexes with metal-metal bonding. Science *375*, 198–202.
25. Lunghi, A., Totti, F., Sanvito, S., and Sessoli, R. (2017). Intra-molecular origin of the spin-phonon coupling in slow-relaxing molecular magnets. Chem. Sci. *8*, 6051–6059.
26. Scherthan, L., Pfleger, R.F., Auerbach, H., Hochdörffer, T., Wolny, J.A., Bi, W., Zhao, J., Hu, M.Y., Alp, E.E., Anson, C.E., et al. (2020). Exploring the Vibrational Side of Spin-Phonon Coupling in Single-Molecule Magnets via 161 Dy Nuclear Resonance Vibrational Spectroscopy. Angew. Chem. Int. Ed. *59*, 8818–8822.
27. Kahn, O. (1993). Molecular Magnetism, 1st edn. (VCH).
28. Gatteschi, D., Sessoli, R., and Villain, J. (2006). Molecular Nanomagnets (Oxford University Press).
29. Swain, A., Sharma, T., and Rajaraman, G. (2023). Strategies to quench quantum tunneling of magnetization in lanthanide single molecule magnets. Chem. Commun. *59*, 3206–3228.
30. Vieru, V., Gómez-Coca, S., Ruiz, E., and Chibotaru, L.F. (2024). Increasing the Magnetic Blocking Temperature of Single-Molecule Magnets. Angew. Chem. Int. Ed. *63*, e202303146.
31. Zhang, H.-L., Zhai, Y.-Q., Qin, L., Ungur, L., Nojiri, H., and Zheng, Y.-Z. (2020). Single-Molecule Toroic Design through Magnetic Exchange Coupling. Matter *2*, 1481–1493.
32. Kaemmerer, H., Baniodeh, A., Peng, Y., Moreno-Pineda, E., Schulze, M., Anson, C.E., Wernsdorfer, W., Schnack, J., and Powell, A.K. (2020). Inorganic Approach to Stabilizing Nanoscale Toroidicity in a Tetraicosanuclear Fe18Dy6 Single Molecule Magnet. J. Am. Chem. Soc. *142*, 14838–14842.
33. Luzon, J., Bernot, K., Hewitt, I.J., Anson, C.E., Powell, A.K., and Sessoli, R. (2008). Spin chirality in a molecular dysprosium triangle: the archetype of the noncollinear ising model. Phys. Rev. Lett. *100*, 247205.
34. Chibotaru, L.F., Ungur, L., and Soncini, A. (2008). The origin of nonmagnetic Kramers doublets in the ground state of dysprosium triangles: evidence for a toroidal magnetic moment. Angew. Chem. Int. Ed. *47*, 4126–4129.
35. Vignesh, K.R., and Rajaraman, G. (2021). Strategies to Design Single-Molecule Toroics Using Triangular {Ln3} n Motifs. ACS Omega *6*, 32349–32364.

36. Li, X.-L., and Tang, J. (2019). Recent developments in single-molecule toroics. Dalton Trans. *48*, 15358–15370.

37. Ungur, L., Lin, S.-Y., Tang, J., and Chibotaru, L.F. (2014). Single-molecule toroics in Ising-type lanthanide molecular clusters. Chem. Soc. Rev. *43*, 6894–6905.

38. Spaldin, N.A., Fiebig, M., and Mostovoy, M. (2008). The toroidal moment in condensed-matter physics and its relation to the magnetoelectric effect. J. Phys. Condens. Matter *20*, 434203.

39. Amoretti, G., Caciuffo, R., Carretta, S., Guidi, T., Magnani, N., and Santini, P. (2008). Inelastic neutron scattering investigations of molecular nanomagnets. Inorg. Chim. Acta. *361*, 3771–3776.

40. Furrer, A., and Waldmann, O. (2013). Magnetic cluster excitations. Rev. Mod. Phys. *85*, 367–420.

41. Garlatti, E., Chiesa, A., Guidi, T., Amoretti, G., Santini, P., and Carretta, S. (2019). Unravelling the Spin Dynamics of Molecular Nanomagnets with Four-Dimensional Inelastic Neutron Scattering. Eur. J. Inorg. Chem. *2019*, 1106–1118.

42. Vonci, M., Giansiracusa, M.J., van den Heuvel, W., Gable, R.W., Moubaraki, B., Murray, K.S., Yu, D., Mole, R.A., Soncini, A., and Boskovic, C. (2017). Magnetic Excitations in Polyoxotungstate-Supported Lanthanoid Single-Molecule Magnets: An Inelastic Neutron Scattering and ab Initio Study. Inorg. Chem. *56*, 378–394.

43. Dunstan, M.A., Cagnes, M., Phonsri, W., Murray, K.S., Mole, R.A., and Boskovic, C. (2022). Magnetic properties and neutron spectroscopy of lanthanoid-{tetrabromocatecholate/18-crown-6} single-molecule magnets. Aust. J. Chem. *75*, 595–609.

44. Atkin, A.M., Giansiracusa, M.J., Calvello, S., Rousset, E., Gable, R.W., Phonsri, W., Murray, K.S., Howard, J.K., Soncini, A., Mole, R.A., and Boskovic, C. (2023). Inelastic Neutron Scattering Measurement of the Ground State Tunneling Gap in Tb and Ho Analogues of a Dy Field-Induced Single-Molecule Magnet. Inorg. Chem. *62*, 1141–1155.

45. Bonde, N.A., Petersen, J.B., Sørensen, M.A., Nielsen, U.G., Fåk, B., Rols, S., Ollivier, J., Weihe, H., Bendix, J., and Perfetti, M. (2020). Importance of Axial Symmetry in Elucidating Lanthanide-Transition Metal Interactions. Inorg. Chem. *59*, 235–243.

46. Baker, M.L., Tanaka, T., Murakami, R., Ohira-Kawamura, S., Nakajima, K., Ishida, T., and Nojiri, H. (2015). Relationship between Torsion and Anisotropic Exchange Coupling in a Tb(III)-Radical-Based Single-Molecule Magnet. Inorg. Chem. *54*, 5732–5738.

47. Giansiracusa, M.J., Moreno-Pineda, E., Hussain, R., Marx, R., Martínez Prada, M., Neugebauer, P., Al-Badran, S., Collison, D., Tuna, F., van Slageren, J., et al. (2018). Measurement of Magnetic Exchange in Asymmetric Lanthanide Dimetallics: Toward a Transferable Theoretical Framework. J. Am. Chem. Soc. *140*, 2504–2513.

48. Prša, K., Nehrkorn, J., Corbey, J., Evans, W., Demir, S., Long, J., Guidi, T., and Waldmann, O. (2016). Perspectives on Neutron Scattering in Lanthanide-Based Single-Molecule Magnets and a Case Study of the Tb2(μ-N2) System. Magnetochemistry *2*, 45.

49. Dunstan, M.A., Mole, R.A., and Boskovic, C. (2019). Inelastic Neutron Scattering of Lanthanoid Complexes and Single-Molecule Magnets. Eur. J. Inorg. Chem. *2019*, 1090–1105.

50. Basler, R., Chaboussant, G., Sieber, A., Andres, H., Murrie, M., Kögerler, P., Bögge, H., Crans, D.C., Krickemeyer, E., Janssen, S., et al. (2002). Inelastic neutron scattering on three mixed-valence dodecanuclear polyoxovanadate clusters. Inorg. Chem. *41*, 5675–5685.

51. Klokishner, S.I., Ostrovsky, S.M., Reu, O.S., Palii, A.V., Tregenna-Piggott, P.L.W., Brock-Nannestad, T., Bendix, J., and Mutka, H. (2009). Magnetic Anisotropy in the [Cu II LTb III (hfac) 2] 2 Single Molecule Magnet: Experimental Study and Theoretical Modeling. J. Phys. Chem. C *113*, 8573–8582.

52. Dreiser, J., Pedersen, K.S., Piamonteze, C., Rusponi, S., Salman, Z., Ali, M.E., Schau-Magnussen, M., Thuesen, C.A., Piligkos, S., Weihe, H., et al. (2012). Direct observation of a ferri-to-ferromagnetic transition in a fluoride-bridged 3d–4f molecular cluster. Chem. Sci. *3*, 1024–1032.

53. Rosado Piquer, L., and Sañudo, E.C. (2015). Heterometallic 3d-4f single-molecule magnets. Dalton Trans. *44*, 8771–8780.

54. Peng, Y., and Powell, A.K. (2021). What do 3d-4f butterflies tell us? Coord. Chem. Rev. *426*, 213490.

55. Liu, K., Shi, W., and Cheng, P. (2015). Toward heterometallic single-molecule magnets: Synthetic strategy, structures and properties of 3d–4f discrete complexes. Coord. Chem. Rev. *289–290*, 74–122.

56. Peng, Y., Mereacre, V., Anson, C.E., and Powell, A.K. (2016). Multiple superhyperfine fields in a {DyFe2Dy} coordination cluster revealed using bulk susceptibility and (57)Fe Mössbauer studies. Phys. Chem. Chem. Phys. *18*, 21469–21480.

57. Peng, Y., Mereacre, V., Anson, C.E., and Powell, A.K. (2018). Butterfly M2IIIEr2 (MIII = Fe and Al) SMMs: Synthesis, Characterization, and Magnetic Properties. ACS Omega *3*, 6360–6368.

58. Vieru, V., Ungur, L., Cemortan, V., Sukhanov, A., Baniodeh, A., Anson, C.E., Powell, A.K., Voronkova, V., and Chibotaru, L.F. (2018). Magnetization Blocking in Fe2III Dy2III Molecular Magnets: Ab Initio Calculations and EPR Spectroscopy. Chemistry (Weinheim an der Bergstrasse, Germany) *24*, 16652–16661.

59. Baniodeh, A., Mereacre, V., Magnani, N., Lan, Y., Wolny, J.A., Schünemann, V., Anson, C.E., and Powell, A.K. (2013). Para versus meta ligand substituents as a means of directing magnetic anisotropy in Fe2Dy2 coordination clusters. Chem. Commun. *49*, 9666–9668.

60. Peng, Y., Singh, M.K., Mereacre, V., Anson, C.E., Rajaraman, G., and Powell, A.K. (2019). Mechanism of magnetisation relaxation in {MIII2DyIII2} (M = Cr, Mn, Fe, Al) "Butterfly" complexes: how important are the transition metal ions here? Chem. Sci. *10*, 5528–5538.

61. Baniodeh, A., Lan, Y., Novitchi, G., Mereacre, V., Sukhanov, A., Ferbinteanu, M., Voronkova, V., Anson, C.E., and Powell, A.K. (2013). Magnetic anisotropy and exchange coupling in a family of isostructural Fe(III)2Ln(III)2 complexes. Dalton Trans. *42*, 8926–8938.

62. Gupta, S.K., Nielsen, H.H., Thiel, A.M., Klahn, E.A., Feng, E., Cao, H.B., Hansen, T.C., Lelièvre-Berna, E., Gukasov, A., Kibalin, I., et al. (2023). Multi-Technique Experimental Benchmarking of the Local Magnetic Anisotropy of a Cobalt(II) Single-Ion Magnet. JACS Au *3*, 429–440.

63. Klahn, E.A., Thiel, A.M., Degn, R.B., Kibalin, I., Gukassov, A., Wilson, C., Canaj, A.B., Murrie, M., and Overgaard, J. (2021). Magnetic anisotropies of Ho(III) and Dy(III) single-molecule magnets experimentally determined via polarized neutron diffraction. Dalton Trans. *50*, 14207–14215.

64. Ridier, K., Gillon, B., Gukasov, A., Chaboussant, G., Cousson, A., Luneau, D., Borta, A., Jacquot, J.-F., Checa, R., Chiba, Y., et al. (2016). Polarized Neutron Diffraction as a Tool for Mapping Molecular Magnetic Anisotropy: Local Susceptibility Tensors in Co(II) Complexes. Chem. Eur J. *22*, 724–735.

65. Ridier, K., Mondal, A., Boilleau, C., Cador, O., Gillon, B., Chaboussant, G., Le Guennic, B., Costuas, K., and Lescouëzec, R. (2016). Polarized Neutron Diffraction to Probe Local Magnetic Anisotropy of a Low-Spin Fe(III) Complex. Angew. Chem. Int. Ed. *55*, 3963–3967.

66. Gao, C., Genoni, A., Gao, S., Jiang, S., Soncini, A., and Overgaard, J. (2020). Observation of the asphericity of 4f-electron density and its relation to the magnetic anisotropy axis in single-molecule magnets. Nat. Chem. *12*, 213–219.

67. Comba, P., Rajaraman, G., Sarkar, A., and Velmurugan, G. (2022). What controls the magnetic anisotropy in heptacoordinate high-spin cobalt(II) complexes? A theoretical perspective. Dalton Trans. *51*, 5175–5183.

68. Neese, F., Atanasov, M., Bistoni, G., Maganas, D., and Ye, S. (2019). Chemistry and Quantum Mechanics in 2019: Give Us Insight and Numbers. J. Am. Chem. Soc. *141*, 2814–2824.

69. Ungur, L., and Chibotaru, L.F. (2017). Ab Initio Crystal Field for Lanthanides. Chem. Eur J. *23*, 3708–3718.

70. Edmonds, A.R. (1957). Angular Momentum in Quantum Mechanics (Princeton University Press).
71. Waldmann, O., and Güdel, H.U. (2005). Many-spin effects in inelastic neutron scattering and electron paramagnetic resonance of molecular nanomagnets. Phys. Rev. B *72*, 094422.
72. Waldmann, O. (2003). Q dependence of the inelastic neutron scattering cross section for molecular spin clusters with high molecular symmetry. Phys. Rev. B *68*, 174406.
73. Marshall, W., and Lovesey, S.W. (1971). Theory of Thermal Neutron Scattering. The Use of Neutrons for the Investigation of Condensed Matter (Clarendon Press).
74. Rechkemmer, Y., Fischer, J.E., Marx, R., Dörfel, M., Neugebauer, P., Horvath, S., Gysler, M., Brock-Nannestad, T., Frey, W., Reid, M.F., and van Slageren, J. (2015). Comprehensive Spectroscopic Determination of the Crystal Field Splitting in an Erbium Single-Ion Magnet. J. Am. Chem. Soc. *137*, 13114–13120.
75. Ishikawa, N., Sugita, M., Okubo, T., Tanaka, N., Iino, T., and Kaizu, Y.. Determination of ligand-field parameters and f-electronic structures of double-decker bis(phthalocyaninato)lanthanide complexes. Inorg. Chem. *42*, 2440–2446.
76. Comba, P., Enders, M., Großhauser, M., Hiller, M., Klingeler, R., Koo, C., Müller, D., Rajaraman, G., Swain, A., Tavhelidse, M., and Wadepohl, H. (2021). Validation of Ab-Initio-Predicted Magnetic Anisotropies and Magneto-structural Correlations in Linear Hetero-trinuclear DyIII -NiII2 Compounds. Chem. Eur J. *27*, 9372–9382.
77. Jensen, J., and Mackintosh, A. (1991). Rare Earth Magnetism. Structures and Excitations (Clarendon Press).
78. Carlin, R.L. (1963). Introduction to ligand field theory (Ballhausen. Carl J.). J. Chem. Educ. *40*, 390.
79. Abragam, A., and Bleaney, B. (1970). Electron Paramagnetic Resonance of Transition Ions (Oxford Univ. Press).
80. Mutschler, J., Ruppert, T., Strahringer, J., Schlittenhardt, S., Ali, Z.A., Peng, Y., Anson, C.E., Ruben, M., Powell, A.K., and Waldmann, O. (2025). Transferability of Ligand Field Parameters in a Family of 3d-4f M2Ln2 Butterfly Single-Molecule Magnets. Inorg. Chem. *64*, 6115–6124.
81. Sievers, J. (1982). Asphericity of 4f-shells in their Hund's rule ground states. Z. Physik B -. Condensed Matter *45*, 289–296.
82. Mitchell, K.J., Abboud, K.A., and Christou, G. (2016). Magnetostructural Correlation for High-Nuclearity Iron(III)/Oxo Complexes and Application to Fe5, Fe6, and Fe8 Clusters. Inorg. Chem. *55*, 6597–6608.
83. Vonci, M., Giansiracusa, M.J., Gable, R.W., van den Heuvel, W., Latham, K., Moubaraki, B., Murray, K.S., Yu, D., Mole, R.A., Soncini, A., and Boskovic, C. (2016). Ab initio calculations as a quantitative tool in the inelastic neutron scattering study of a single-molecule magnet analogue. Chem. Commun. *52*, 2091–2094.
84. Gysler, M., El Hallak, F., Ungur, L., Marx, R., Hakl, M., Neugebauer, P., Rechkemmer, Y., Lan, Y., Sheikin, I., Orlita, M., et al. (2016). Multitechnique investigation of Dy3 - implications for coupled lanthanide clusters. Chem. Sci. *7*, 4347–4354.
85. Ollivier, J., and Mutka, H. (2011). IN5 Cold Neutron Time-of-Flight Spectrometer, Prepared to Tackle Single Crystal Spectroscopy. J. Phys. Soc. Jpn. *80*, SB003.
86. Mutschler, J., Ollivier, J., Peng, Y., and Waldmann, O. (2019). Studying the Magnetic Properties of a Heterometallic Single Molecule Magnet Series Containing Transition Metal and Rare Earth Ions with INS. Institut Laue-Langevin (ILL). https://doi.org/10.5291/ILL-DATA.4-06-9.
87. Mutschler, J., Ollivier, J., Ruppert, T., and Waldmann, O. (2020). Study of a Novel Series of Isostructural Heterometallic 3d-4f Single Molecule Magnets with INS. Institut Laue-Langevin (ILL). https://doi.org/10.5291/ILL-DATA.4-06-11.
88. Arnold, O., Bilheux, J.C., Borreguero, J.M., Buts, A., Campbell, S.I., Chapon, L., Doucet, M., Draper, N., Ferraz Leal, R., Gigg, M.A., et al. (2014). Mantid—Data analysis and visualization package for neutron scattering and μ SR experiments. Nucl. Instrum. Methods Phys. Res. Sect. A Accel. Spectrom. Detect. Assoc. Equip. *764*, 156–166.